Title	Effects of hydrogen ion irradiation on zinc oxide etching
Author(s)	Li, Hu; Karahashi, Kazuhiro; Friederich, Pascal et al.
Citation	Journal of Vacuum Science and Technology A: Vacuum, Surfaces and Films. 2017, 35(5), p. 05C303
Version Type	VoR
URL	https://hdl.handle.net/11094/78460
rights	This article may be downloaded for personal use only. Any other use requires prior permission of the author and AIP Publishing. This article appeared in Journal of Vacuum Science & Technology A 35, 05C303 (2017) and may be found at https://doi.org/10.1116/1.4982715.
Note	

Effects of hydrogen ion irradiation on zinc oxide etching

Hu Li, Kazuhiro Karahashi, Pascal Friederich, Karin Fink, Masanaga Fukasawa, Akiko Hirata, Kazunori Nagahata, Tetsuya Tatsumi, Wolfgang Wenzel, and Satoshi Hamaguchi

View Online   Export Citation   CrossMark

Effects of hydrogen ion irradiation on zinc oxide etching

Hu Li and Kazuhiro Karahashi
Center for Atomic and Molecular Technologies, Osaka University, 2-1 Yamadaoka, Suita, Osaka 565-0871, Japan

Pascal Friederich and Karin Fink
Institute of Nanotechnology, Karlsruhe Institute of Technology (KIT), Hermann-von-Helmholtz-Platz 1, Eggenstein-Leopoldshafen 76344, Germany

Masanaga Fukasawa, Akiko Hirata, Kazunori Nagahata, and Tetsuya Tatsumi
Sony Semiconductor Solutions Corporation, 4-14-1 Asahi-cho, Atsugi, Kanagawa 243-0014, Japan

Wolfgang Wenzel
Institute of Nanotechnology, Karlsruhe Institute of Technology (KIT), Hermann-von-Helmholtz-Platz 1, Eggenstein-Leopoldshafen 76344, Germany

Satoshi Hamaguchi[a]
Center for Atomic and Molecular Technologies, Osaka University, 2-1 Yamadaoka, Suita, Osaka 565-0871, Japan

Mechanisms of zinc oxide (ZnO) etching by hydrocarbon plasmas were investigated both experimentally and theoretically with the use of a mass-selected ion beam system and first-principle quantum mechanical (QM) simulation based on the density functional theory. The mass-selected ion beam experiments have shown that the sputtering yield of ZnO increases by a pretreatment of the ZnO film by energetic hydrogen (H) ion injections prior to heavy ion bombardment, suggesting that chemically enhanced etching of ZnO by hydrocarbon plasmas is closely related to hydrogen storage and/or formation of damage in the ZnO layer by energetic hydrogen injections. In this study, the effects of hydrogen storage in ZnO are examined. First-principle QM simulation of ZnO interacting with H atoms has shown that H atoms in ZnO form hydroxyl (OH) groups (or partially convert ZnO to ZnOH), which results in the weakening or breaking of the Zn–O bonds around H atoms and thus makes the ZnO film more prone to physical sputtering. The formation of hydroxyl groups in ZnO is also expected to occur in ZnO etching by hydrocarbon plasmas and increase its sputtering yields over those by inert-gas plasmas generated under similar conditions. © *2017 American Vacuum Society*. [http://dx.doi.org/10.1116/1.4982715]

I. INTRODUCTION

Zinc oxide (ZnO) is a transparent conducting oxide (TCO) that may be used as an alternative to indium tin oxide for microelectronics devices. As the sizes of some microelectronics devices using TCOs decrease, there has been an increasing demand for submicron- or even nanoscale pattern formation of ZnO thin films deposited on Si wafers. Reactive ion etching (RIE), which uses synergetic effects of chemical reactions and ion bombardment, may be applied to ZnO etching processes. Hydrocarbon or similar gases such as methane (CH_4) and methanol (CH_3OH) are indeed favorable choices for RIE of ZnO because of their noncorrosive chemistry and reasonably high etching rates.[1–16] A better understanding of etching reaction mechanisms of ZnO in RIE processes based on such gases is expected to facilitate the development of highly controlled submicron- and nanoscale etching processes of ZnO.

Many studies on RIE processes of Si-based semiconductor devices have shown that a modification or pretreatment of a Si surface by incident hydrogen (H) radicals or energetic hydrogen ions (H^+ ions) strongly affects the etching properties of Si by subsequent heavy ion bombardment.[17–24] The impact of energetic H^+ ions may not etch Si so much because of their low mass but often induces damages to the crystalline structure of Si as they penetrate into the film to a relatively large depth.[23,24] As to ZnO, the effects of hydrogen in ZnO have been widely studied since the presence of hydrogen in ZnO affects the structural, optical, and electrical properties of ZnO.[25–34] It is therefore conjectured that the penetration of H^+ ions into ZnO during the etching process may affect its etching properties. Indeed, our earlier study[35] has shown that chemically enhanced etching of ZnO occurs by energetic CH_3^+ ion impact whereas carbon tends to accumulate on a ZnO surface by energetic CH^+ ion impact. However, this earlier study did not clarify how hydrogen of the incident ions affected the sputtering yields of ZnO.

When energetic H^+ ions are injected into a ZnO film, they are likely to damage the microcrystalline structures near its top surface and also be stored as H atoms in the ZnO film, possibly forming hydroxyl (OH) groups in ZnO. Our goal is to clarify the effects of incident hydrogen on etching reactions of ZnO. In this study, we focus on examining how stored hydrogen in ZnO may modify the atomic-scale structures of ZnO and affect its sputtering yields. To achieve this goal, we use ion beam injection experiments to observe the

[a]Electronic mail: hamaguch@ppl.eng.osaka-u.ac.jp

surface modification of ZnO by H^+ ion injections and first-principle quantum mechanical (QM) simulation to evaluate the changes of bond energies of ZnO in the presence of H atoms. The effects of the damage formation in ZnO by energetic H^+ ion injections on its etching properties are a subject of future study.

II. EXPERIMENTAL METHODS

The mass selected ion beam system[35–44] used in this study can inject mass-selected ions with a specified energy. A schematic diagram of the ion beam system is given in Fig. 1. Only desired ion species such as Ar^+ or CH_3^+, which are generated in the ion source, are selected by the analyzing magnet. The ion beam energy is adjusted to the desired incident energy by a series of electrodes set along the beamline before the beam ions reach the sample surface. The characteristics of the ion beam, i.e., ion species and their incident energy, are identified and monitored by a quadrupole mass spectroscopy (QMS) with an energy analyzer set in the reaction chamber.

The ZnO sample used in this study is a film with a thickness of about 2000 Å, measured by ellipsometry, formed on a 1.6×1.6 cm square Si chip by sputter deposition. The atomic compositions are 45.1% Zn and 54.9% O with the total atomic number density being 7.9×10^{22} cm^{-3}, measured by Rutherford backscattering spectrometry.

The sputtering yield of ZnO in this study is defined as the total number of desorbed Zn and O atoms per incident ion. The sputtering yield was derived from the depth profile of the etched ZnO surface measured by a surface profiler (Dektak3ST) and the ion dose. To achieve accurate measurement of depth profiles, we used a metal stencil mask placed on the sample surface

during beam irradiation.[36] The conversion of the etched depth to the total number of Zn and O atoms removed from the surface was done with use of the atomic number density of ZnO, i.e., 7.9×10^{22} cm^{-3}, given above. The ion dose was estimated from the ion current and beam irradiation time. The ion current was measured with a Faraday cup before and after each ion irradiation experiment.

The chemical compositions of a sample surface before and after beam exposure may be analyzed with an *in situ* x-ray photoelectron spectroscopy (XPS) system installed in the reaction chamber. In this study, we also analyzed the composition of the ZnO surface by *ex situ* secondary ion mass spectrometry (SIMS) after ion beam injection. (The sample was taken outside from the high vacuum reaction chamber of the ion beam system prior to the SIMS measurement.) In SIMS measurement, 5 keV Cs^+ ions were focused on to the ZnO surface to ionize and sputter the atoms from the surface.

III. EXPERIMENTAL RESULTS

Figure 2 shows the Auger electron spectra (AES) from ZnO surfaces before and after ion beam injections measured by the *in situ* XPS system. In all ion beam experiments performed in this study, the angle of ion beam incidence was normal to the sample surface. The surface contamination was removed by Ar^+ ion bombardment with 500 eV prior to H^+ ion injection. We used a molybdenum (Mo) mask to cover the ZnO surface during the ion beam injections and the AES measurement. The Mo mask had a hole with a diameter of 5 mm and ion beam was injected uniformly into the entire uncovered part of the ZnO surface. Then, the ZnO sample with the Mo mask was exposed to X-rays of the XPS system for the AES measurement.
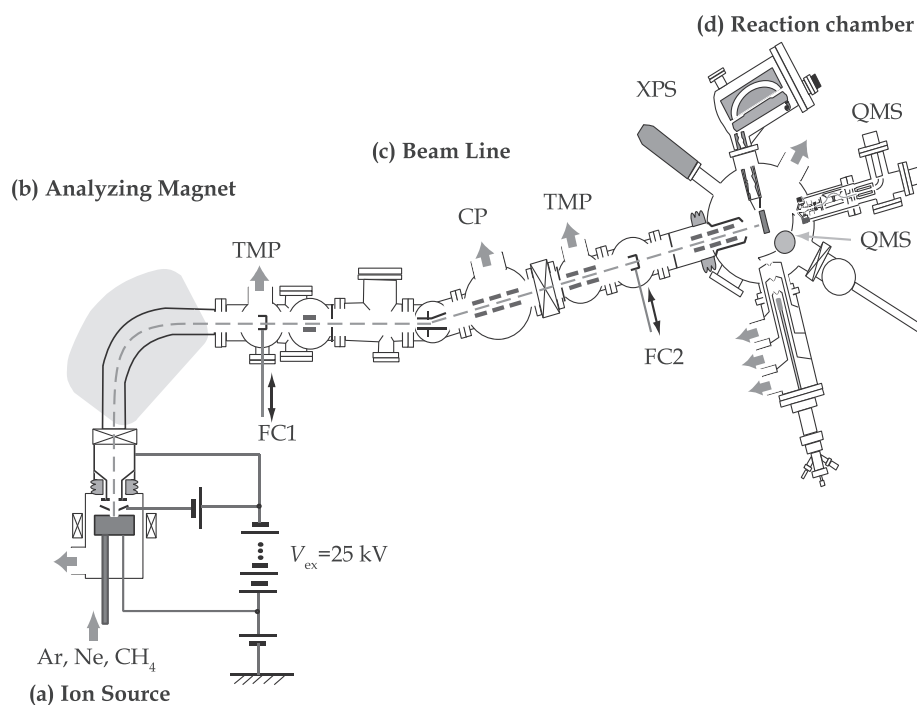

Fig. 1. Schematic view of the mass-selected ion beam system. The system consists of (1) ion source, (2) analyzing magnet, (3) beam line, and (4) reaction chamber. TMP: turbomolecular pump, CP: cryogenic pump, XPS: x-ray photoelectron spectroscopy, QMS: quadrupole mass spectrometer, and FC: Faraday cup.
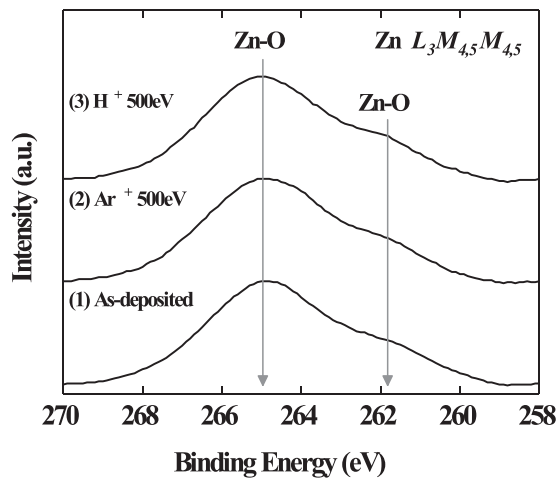
FIG. 2. Zn $L_3M_{4,5}M_{4,5}$ Auger electron spectra from (1) an as-deposited ZnO surface, (2) a cleaned ZnO surface, i.e., a surface after 500 eV Ar$^+$ ion injection into the as-deposited ZnO surface, and (3) a cleaned ZnO surface exposed to 500 eV H$^+$ ion injection with an ion dose of 1×10^{17}/cm^2.

The spectra from an as-deposited ZnO surface were measured as a reference. Two peaks at bonding energies of 265.1 and 261.8 eV, which correspond to the Zn–O bond, were observed. No change was seen in spectra between the cleaned and as-deposited surfaces, indicating that the surface stoichiometry did not change by the 500 eV Ar$^+$ ion bombardment. The spectra from the 500 eV H$^+$ ion-irradiated surface also exhibited no change. The ion doses of Ar$^+$ and H$^+$ ions in Fig. 2 were approximately 5×10^{16} and 1×10^{17}/cm^2. It is clearly seen that the ZnO surface was not reduced by the injection of H$^+$ ions. Similar phenomena were also observed in earlier studies.[45,46]

Figure 3 shows the *ex situ* SIMS measurement of hydrogen concentrations in a ZnO layer after 500 eV H$^+$ ion injection. It clearly shows a high concentration of hydrogen in the near surface region ($\sim$30 nm). These results suggest that hydrogen can be stored in a ZnO layer without surface reduction and form a hydrogen-rich layer. Some earlier studies also have shown an incorporation of hydrogen in ZnO.[6] The depth shown in Fig. 3 is calculated from the number of Zn and O atoms observed per
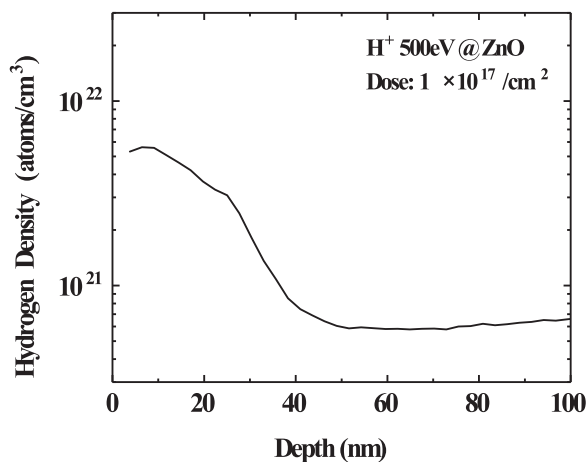
unit time in SIMS and the known density of crystalline ZnO. It is seen in Fig. 3 that the atomic percentage of hydrogen in ZnO is about 6% near the top surface as the atomic number density of the ZnO film is 7.9×10^{22} cm^{-3}, as mentioned earlier.

Figure 4 shows the sputtering yields of ZnO by Ne$^+$ ions as functions of the Ne$^+$ ion incident energy before and after the ZnO film is exposed to energetic H$^+$ ions, obtained from ion beam experiments. In the latter case, the ZnO sample was exposed to a 500 eV H$^+$ ion beam with an ion dose of 1×10^{17}/cm^2 prior to the exposure to Ne$^+$ ions. The sputtering yield data of ZnO by Ne$^+$ and CH$_3^+$ ions (without H$^+$ ion pretreatments) in Fig. 4 are the same as those presented in Ref. 35. It is seen that the physical sputtering yield of ZnO by Ne$^+$ ions increases significantly after it is exposed to energetic H$^+$ ions. It should be noted that, in evaluating the sputtering yields, we assumed for the sake of simplicity that the atomic density of the ZnO film did not change after it was exposed to the 500 eV H$^+$ ion beam.

Since the masses and sizes of C and Ne atoms are similar, the physical sputtering yields of any material by C$^+$ ions and Ne$^+$ ions should be similar. Assuming that similar modifications of ZnO by hydrogen occur by incident CH$_3^+$ ions and 500 eV H$^+$ ions upon the film surfaces and carbon hardly react with hydrogen modified ZnO, we expect the sputtering yields of ZnO by CH$_3^+$ ions and hydrogen-modified ZnO by Ne$^+$ ions are similar. Thus Fig. 4, which indeed shows nearly the same sputtering yields of ZnO by CH$_3^+$ ions and hydrogen-pretreated ZnO by Ne$^+$ ions, suggests that the energetic impact of CH$_3^+$ ions on the ZnO surface simultaneously modifies it with their H atoms and physically sputter it by their heavier C atoms.

As mentioned earlier, when energetic H$^+$ ions are injected into a ZnO film, they are likely to damage the microcrystalline structures near its top surface and may increase its sputtering yield. Such effects are beyond the scope of the current work and deferred to future study. In Secs. IV and V, we

FIG. 3. Depth profile of hydrogen density of a cleaned ZnO surface exposed to 500 eV H$^+$ ions with an ion dose of 1×10^{17}/cm^2, obtained from SIMS.
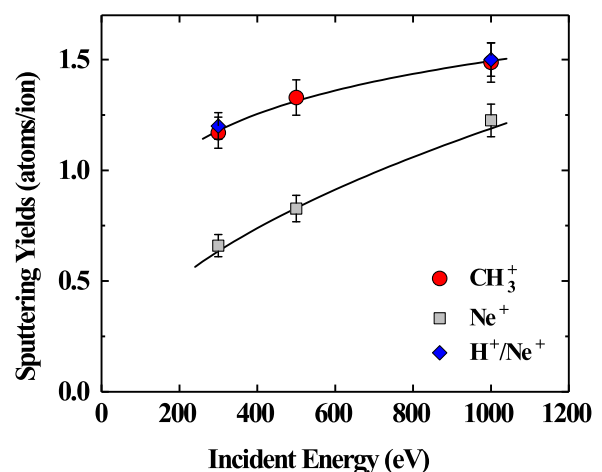
FIG. 4. (Color online) Sputtering yields of ZnO by Ne$^+$ ions (from Ref. 35) and the sputtering yields by Ne$^+$ ions of a ZnO film exposed to 500 eV H$^+$ ions with an ion dose of 1×10^{17}/cm^2 prior to Ne$^+$ ion exposure. The sputtering yield of ZnO is defined as the total number of Zn and O atoms removed from the surface per incident ion. It is seen that the H$^+$ ion treatment of ZnO significantly increases its physical sputtering yield by Ne$^+$ ions. Solid curves are guides to the eye.

FIG. 5. (Color online) Side view of a rectangular ZnO hexagonal wurtzite crystal with the top surface representing a (10$\bar{1}$0) ZnO surface, used in our simulation. A large sphere and a small spher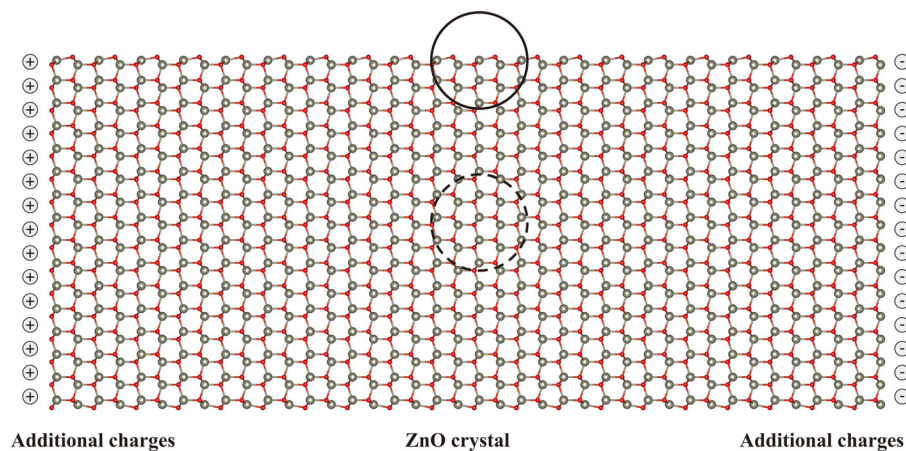e represent Zn and O atoms. DFT simulation is performed only for a small cluster of atoms placed in the central region (called the QM region) of this system, which is approximately denoted by the solid or broken circle. Since no periodic boundary condition is imposed, additional counter-charges are also placed on both sides of the crystal to eliminate the global dipole moment arising from positively charged Zn atoms on one side and negatively charged O atoms on the other side.

shall discuss how stored hydrogen can affect atomic structures of ZnO and the resistance of ZnO against physical sputtering, using QM simulation based on the density functional theory (DFT).

IV. COMPUTATIONAL METHODS

In this section, we describe how DFT calculations can be used to evaluate the modification of bond energies of

ZnO crystals by additional H atoms. To examine this local effect, we use the embedded cluster method (ECM)[47] to evaluate a small region of a ZnO crystal in DFT. In this method, a large but finite ZnO crystal (hexagonal wurtzite), as shown in Fig. 5, is taken as a model system. Figure 5 shows a side view of such a model system, i.e., a rectangular ZnO crystal with the top surface representing a (10$\bar{1}$0) surface. The lattice parameters for the unit cell are obtained from Ref. 47.

(a)

(b)

(c)

(d)
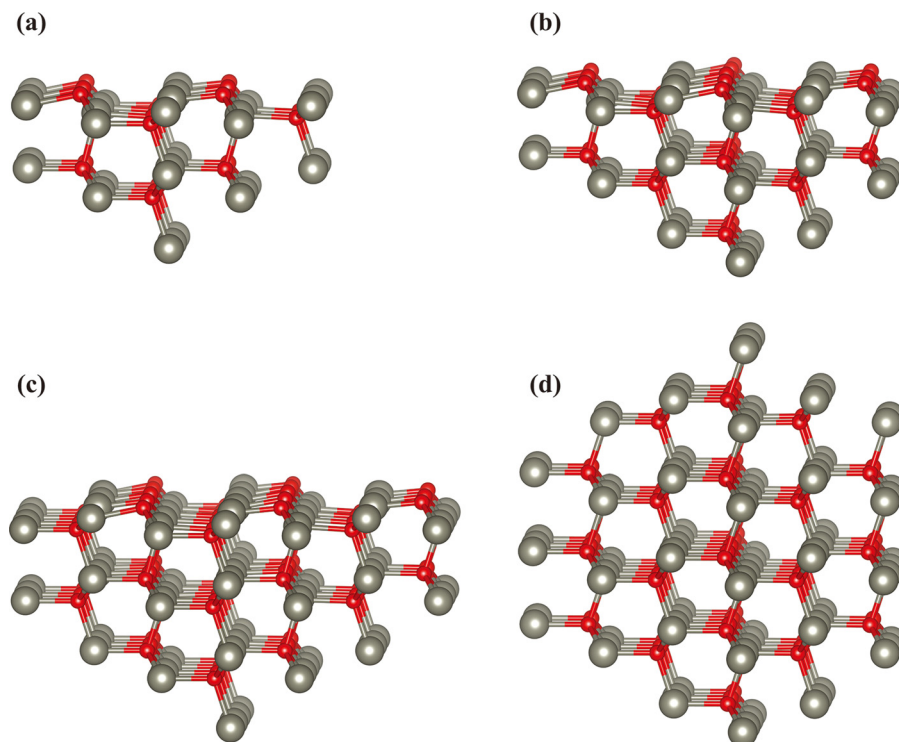
FIG. 6. (Color online) Configurations of optimized structure of various sizes of ZnO clusters and their surrounding Zn atoms represented by ECPs. The corresponding ZnO clusters in the QM region are (a) Zn_9O_{19}, (b) $Zn_{19}O_{36}$, (c) $Zn_{36}O_{58}$, and (d) $Zn_{29}O_{57}$. It should be noted that Zn atoms in the outermost layer depicted in each atomic configuration here are the ones represented by ECPs and their positions are fixed during structure optimization. The clusters (a), (b), and (c) were used for surface simulation whereas the cluster (d) was used for bulk simulation in this study. More detailed information on each cluster and its surrounding ECPs that represent Zn atoms of the outermost layer is given in Table I.

In the ECM, the entire system is divided into two regions: the QM region, where atoms are treated quantum-mechanically, and the embedding region, where atoms are essentially represented only by point charges (PCs), i.e., $+2e$ for Zn and $-2e$ for O, located at the crystalline lattice sites. Here, e denotes the elementary charge. In case a cluster of the QM region is terminated by a layer of O atoms, Zn atoms of the surrounding outer layer in the embedding region are represented not by simple $+2e$ PCs but by electron pseudo-potentials, which are also called electron core potentials (ECPs). The ECPs serve as additional embedding potentials to prevent leakage of the electron density of the negatively charged O atoms. When surface properties of ZnO are studied, the QM region is placed around the center of the top surface as approximately indicated by the solid circle in Fig. 5. Similarly, when bulk properties of ZnO are studied, the QM region is placed around the center of the rectangular crystal, as approximately indicated by the broken circle in Fig. 5.

Sample ZnO clusters used in our simulation for the QM region are summarized in Fig. 6 and Table I. We created a cluster of ZnO atoms that are to be simulated quantum-mechanically in the QM region by alternately adding complete shells of Zn or O atoms. If an O (Zn) atom was chosen as the central atom of the cluster, then Zn (O) atoms which tetrahedrally surround the central atom were added in the first

shell. In the next surrounding shells, O (Zn) atoms are added to the cluster in a similar way. If the cluster is part of the top surface, it is cut in half so that a $(10\bar{1}0)$ surface is exposed.

Figure 6(a) represents a schematic atomic arrangement of a Zn_9O_{19} cluster used to simulate the $(10\bar{1}0)$ surface of a ZnO crystal. Large and small spheres represent Zn and O atoms, respectively. The bonds connecting Zn and O atoms are just a guide to the eye, conceptually representing the Zn–O bonds. As indicated in Table I, at the center of the cluster, there is a single Zn atom. This Zn atom is located at the center of the top surface of this cluster. The first half shell that surrounds the central Zn atom consists of three O atoms. The second and third half shells consist of 8 Zn atoms and 16 O atoms, respectively. Note that the 27 Zn atoms at the outer-most shell (the 4th shell) of the cluster shown in Fig. 6(a) only enter the DFT calculation as ECPs (as indicated in Table I). To increase the accuracy of the simulation, we also used larger clusters such as $Zn_{19}O_{36}$ and $Zn_{36}O_{58}$, as shown in Figs. 6(b) and 6(c) and Table I. Figure 6(d) is a $Zn_{29}O_{57}$ cluster that may be used as a small cluster to represent bulk properties of ZnO and placed at the center of the ZnO crystal shown in Fig. 5, around the location indicated by the broken circle. The bottom half of the $Zn_{29}O_{57}$ cluster of (d) is the same as the $Zn_{19}O_{36}$ cluster of (b).

In this study, geometry optimization of the ZnO cluster in the QM region was performed in its DFT simulation[48] based on the resolution-of-the-identity approximation[49,50] with def2-SVP and def2-TZVPP basis sets.[51,52] The outer-most layer of the cluster as well as the position of the embedding ECPs and point charges was kept frozen in geometry optimization.

The finite ZnO crystal shown in Fig. 5 is terminated by a layer of Zn atoms at one side (on the left in this figure) and a layer of O atoms at the other side (on the right). Such terminations create an artificial dipole moment across the crystal. In order to compensate this finite size effect, we place additional counter-charges on both sides of the crystal to eliminate the global dipole moment in this system.[53–55] (These additional counter-charges are not counted as PCs in Table I.) DFT-D3 (Ref. 56) corrections are used to introduce dispersion interactions in the DFT simulation. The exchange-correlation energy is based on the Perdew-Burke-Ernzerhof (PBE) functional.[57–60] All the calculations were performed using the quantum chemistry package TURBOMOLE.[61]

The vacancy formation energy (VFE) may be considered as the minimum energy needed to remove an atom from the

TABLE I. Information on different sizes of ZnO clusters, their surrounding Zn atoms represented by ECPs, and PCs used for ECM-based simulations of this study. The corresponding atomic configurations are given in Fig. 6.

	QM region		ECPs	Numbers	Coordinates
Surface Zn_9O_{19}	Central	Zn		1	
	1st shell	O		3	
	2nd shell	Zn		8	
	3rd shell	O		16	Fixed
	4th shell		Zn	27	Fixed
	PCs			57385	Fixed
Surface $Zn_{19}O_{36}$	Central	O		1	
	1st shell	Zn		3	
	2nd shell	O		8	
	3rd shell	Zn		16	
	4th shell	O		27	Fixed
	5th shell		Zn	39	Fixed
	PCs			57346	Fixed
Surface $Zn_{36}O_{58}$	Central	Zn		1	
	1st shell	O		3	
	2nd shell	Zn		8	
	3rd shell	O		16	
	4th shell	Zn		27	
	5th shell	O		39	Fixed
	6th shell		Zn	54	Fixed
	PCs			57292	Fixed
Bulk $Zn_{29}O_{57}$	Central	O		1	
	1st shell	Zn		4	
	2nd shell	O		12	
	3rd shell	Zn		25	
	4th shell	O		44	Fixed
	5th shell		Zn	67	Fixed
	PCs			57287	Fixed

TABLE II. VFEs to remove a Zn atom, $E_{V(Zn)}$, and an O atom, $E_{th(O)}$, from the $(10\bar{1}0)$ surface of a ZnO film, evaluated from ECM-based DFT simulations with the three different ZnO clusters in the QM region with the two different basis sets.

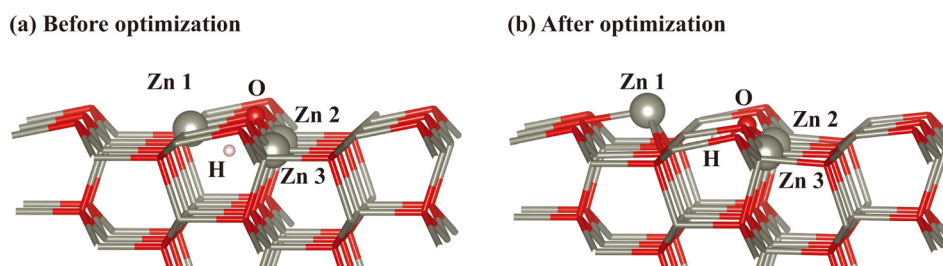| VFEs of a ZnO surface (eV)						
Cluster	Zn_9O_{19}	$Zn_{19}O_{36}$	$Zn_{36}O_{58}$	Zn_9O_{19}	$Zn_{19}O_{36}$	$Zn_{36}O_{58}$
Basis set		def2-SVP			def2-TZVPP	
$E_{V(Zn)}$	6.8	7.1	6.9	6.2	6.2	6.1
$E_{V(O)}$	6.8	6.6	6.4	6.2	6.0	6.0

(a) Before optimization   **(b) After optimization**

FIG. 7. (Color online) Atomic configurations of the $Zn_{19}O_{36}$ cluster of Fig. 6(b) when (a) a H atom is placed at an arbitrary subsurface position around the center of the top surface of the cluster with nearly equal distances from the surrounding Zn and O atoms and (b) after geometrical optimization by DFT simulation based on the ECM. To simply the figure, atoms are represented only by the bond nodes except for some specific Zn atoms on the top surface (denoted as Zn1, Zn2, and Zn3) by a large sphere and a medium-size sphere, and the introduced H atom by a small white sphere. The nodes of light- and dark-toned (online: gray- and red-colored) bonds represent Zn and O atoms, respectively.

material (i.e., form a vacancy). More precisely, the VFE $E_{V(A)}$ of removing an atom A from the material is defined (at zero temperature) using the potential energy $E_{w/oA}$ of the material with a vacancy, the potential energy E_A of isolated atom A removed from the material, and the potential energy of the material without vacancy E as

$$E_{V(A)} = E_{w/oA} + E_A - E.$$

It should be noted that the geometry optimization must be performed in each system, i.e., the systems with and without vacancy. In general, the VFE depends on the position from which a specific atom is removed. In this study, we only focus on the VFE to remove a Zn or O atom located at the very top surface of a crystalline ZnO film.

V. COMPUTATIONAL RESULTS

First, we have evaluated the VFEs of ZnO, using the three ZnO clusters of Figs. 6(a)–6(c) with ECM-based DFT simulations mentioned above. The VFE for a Zn atom, i.e., $E_{V(Zn)}$, and that for an O atom, i.e., $E_{V(O)}$, were evaluated by removing a Zn or O atom in the center or next to the center in each cluster. The results are summarized in Table II. It is seen that the VFEs for Zn and O atoms are similar, meaning that it requires almost the same energy to remove a Zn or O atom from ZnO. This may be easily understood because the numbers of Zn and O atoms are the same in a ZnO crystal, and therefore, the total bond energy of a single Zn atom attached to the surrounding O atoms and that of a single O

atom attached to the surrounding Zn atoms must be the same essentially. This also indicates that the sputtering of Zn and O atoms from a ZnO surface occurs nearly simultaneously, which supports the fact that the unchanged surface stoichiometry observed in our AES measurement after physical sputtering of ZnO by Ar^+ ion bombardment (Fig. 2).

We also evaluate the VFE of ZnO to remove a Zn or O atom located at the top surface in the presence of a charge neutral H atom. As shown in Fig. 7(a), a charge neutral H atom is placed at an arbitrary location slightly below the very top surface, almost equally distanced from the nearby Zn atoms (denoted as Zn1, Zn2, and Zn3) and O atom (denoted as O) forming the very top surface. The ZnO cluster used in this simulation is $Zn_{19}O_{36}$ of Fig. 6 (b).

After geometrical optimization, the H atom moved closer to the O atom and formed an O–H bond by breaking the Zn–O bond, forcing a Zn atom (Zn1) to move away from the O atom, as shown in Fig. 7(b). It should be noted that the atomic percentage of hydrogen in ZnO that we are concerned with is at most about 6%, as shown in Fig. 3, and therefore, H atoms in ZnO are considered to be well separated from each other. Thus, it is consistent with experimental observations to introduce a single H atom (rather than many) in the small QM region for our simulation study.

In the atomic configuration of Fig. 7(b), which is considered to be the most stable state in the presence of a H atom near the surface, the VFEs to remove the Zn atom (denoted as Zn1), the O atom (denoted as O) only, and the hydroxyl group, are evaluated and given in Table III. It is seen that, in the presence of an H atom, it requires less energy to remove

TABLE III. VFEs to remove a Zn atom, $E_{V(Zn)}^H$, an O atom, $E_{V(O)}^H$, and an OH group, $E_{V(OH)}^H$, from the $(10\bar{1}0)$ surface of a ZnO film in the presence of a H atom, evaluated from ECM-based DFT simulations with the two different basis sets. The cluster in the QM region used in these simulations is $Zn_{19}O_{36}$ of Table I.

VFEs of a ZnO surface in the presence of a H atom (eV)

Cluster	$Zn_{19}O_{36}$	
Basis set	def2-SVP	def2-TZVPP
$E_{V(Zn)}^H$	3.6	2.9
$E_{V(O)}^H$	6.7	5.8
$E_{V(OH)}^H$	4.8	2.9

TABLE IV. Charges (in units of elementary charge e) of and bond lengths (in units of Å) among the atoms denoted as Zn1, Zn2, Zn3, O, and H on the $(10\bar{1}0)$ ZnO surface shown in Fig. 7, after geometry optimization by ECM-based DFT simulations with a basis set of def2-SVP for the $Zn_{19}O_{36}$ cluster of Fig. 6 (b) in the absence or presence of an introduced H atom.

Atomic charges (e)			Atomic distances (Å)		
Atom type	Without H	With H	Atom type	Without H	With H
H		0.2197	O − H		0.984
Zn 1	−0.6692	−0.5112	O − Zn 1	2.010	3.082
Zn 2	0.7198	0.7177	O − Zn 2	1.981	1.952
Zn 3	0.7198	0.7178	O − Zn 3	1.981	1.952

TABLE V. Charges (in units of elementary charge e) of and bond lengths (in units of Å) among the atoms denoted as Zn1, Zn2, Zn3, Zn4, O, and H in the bulk of ZnO shown in Fig. 8, after geometry optimization by ECM-based DFT simulations with a basis set of def2-SVP for the $Zn_{29}O_{57}$ cluster of Fig. 6(d) in the absence or presence of an introduced H atom.

Atomic charges (e)			Atomic distances (Å)		
Atom type	Without H	With H	Atom type	Without H	With H
H		0.1605	O − H		0.998
O	−0.7399	−0.5300	O − Zn 1	1.974	2.302
Zn 1	0.8191	0.8320	O − Zn 2	1.974	2.116
Zn 2	0.8191	0.8101	O − Zn 3	1.992	2.156
Zn 3	0.7994	0.7830	O − Zn 4	1.973	2.101
Zn 4	0.8186	0.8114			

the Zn atom from the surface than in the absence of hydrogen. It is also shown that removing an O atom as a hydroxyl group is energetically more favorable than doing so as an individual O atom. These results suggest, in terms of energy levels, that ZnO becomes less resistant to physical sputtering when hydrogen is stored near its top surface.

Table IV shows how hydrogen affects both charge distributions and Zn–O bond lengths. After geometrical optimization, it is shown that the introduced H atom becomes positively charged as a typical H atom of a hydroxyl group whereas the negative charge of the O atom forming the hydroxyl group is reduced as one of its bonds with Zn atoms is broken. It is also seen that the O–H bond length is 0.98 Å, which is a typical O–H bond length found in many familiar systems such as H_2O and methanol.[62] The formation of an O–H chemical bond has also been confirmed by the molecular orbitals (not shown here) formed around the H and O atoms. The simulation results here are consistent with other theoretical and experimental studies[30,32,63] showing that hydrogen forms hydroxyl groups in ZnO. Furthermore, it is shown that the Zn–O bonds near the H atom are elongated due to the repulsive electrostatic forces between H and Zn atoms, both of which are positively charged.

Similar results have been also observed when an H atom is introduced in the bulk of ZnO, as seen in Fig. 8 and Table V. In Fig. 8(a), an H atom is placed at an arbitrary position

near the center of the $Zn_{29}O_{57}$ cluster of Fig. 6 (d) with nearly equal distances from surrounding Zn and O atoms. Figure 8(b) shows the atomic configuration after geometrical optimization by ECM-based DFT simulation.

The simulation results in this section clearly show that, with stored hydrogen, ZnO partially forms ZnOH and its structure becomes less resistant against physical sputtering. However, the results offer only qualitative tendency regarding the sputtering yield of ZnO, and it is not clear at the moment how much the sputtering yield would be increased for a given amount of stored hydrogen. In this study, we only considered the case where deposited hydrogen exists in a crystalline ZnO. This is because ZnO typically forms a microcrystalline structure and we believe that the presence of hydrogen can alter the crystalline structure of its grain (i.e., crystallite) more drastically than the structures of its grain boundaries, where disconnected (i.e., dangling) bonds of oxygen can be easily terminated by inserted hydrogen atoms without much changing the atomic configurations. Many deposited H atoms are likely to be stored in grain boundaries, and we simply did not consider such cases in this study. A quantitative discussion on the change of the ZnO sputtering yield by incident H^+ ions is beyond the scope of this work and is deferred to future study.

VI. CONCLUSIONS

In this study, the mechanisms of chemically enhanced etching of ZnO by hydrogen have been examined with ion beam experiments and first-principle QM simulations. The beam experiments have shown that H^+ ions injected into a ZnO film can be deposited as H atoms inside the film without reducing (i.e., removing oxygen from) the ZnO surface. It has been also found in the beam experiments that the physical sputtering yield of ZnO increases after it is exposed to H^+ ion beam injection. These results indicate that a ZnO film is modified by H^+ ion irradiation and the modified layer has a higher sputtering yield than pure ZnO.

The first-principle QM simulation results have indicated that the deposition of hydrogen in ZnO causes the formation of hydroxyl groups, partially converting ZnO to ZnOH by breaking some Zn–O bonds. The VFEs of ZnO for the
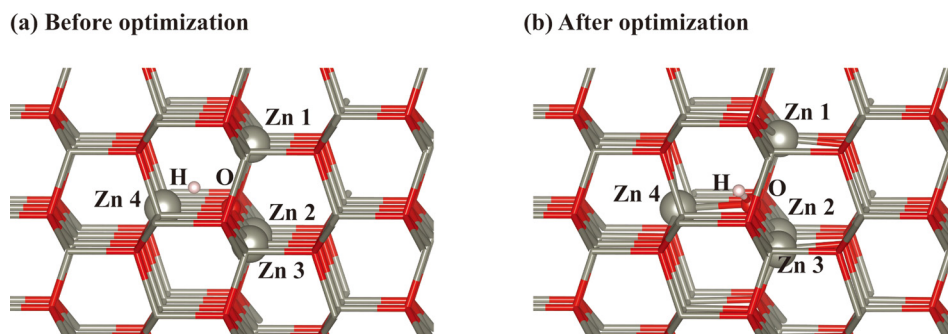
(a) Before optimization   **(b) After optimization**

FIG. 8. (Color online) Atomic configurations of the $Zn_{29}O_{57}$ cluster of Fig. 6(d) when (a) a H atom is placed at an arbitrary position near the center of the cluster with nearly equal distances from the surrounding Zn and O atoms and (b) after geometrical optimization by DFT simulation based on the ECM. To simply the figure, atoms are represented only by the bond nodes except for some specific Zn atoms (denoted as Zn1, Zn2, Zn3, and Zn4) by large spheres, an O atom by a mediium-size sphere, and the introduced H atom by a small white sphere. The nodes of light- and dark-toned (online: gray- and red-colored) bonds represent Zn and O atoms, respectively.

removal of Zn and O atoms are also found to be lower in the presence of H atoms (that form hydroxyl groups) than those of ZnO without H atoms. This is consistent with the experimental observation that a ZnO film modified by H^+ ion beam injection has higher physical sputtering yield by Ne^+ ion bombardment.

The experimental and computational study performed here can also account for the RIE of ZnO by hydrocarbon plasmas. Some incident ions from a hydrocarbon plasma such as CH_3^+ contain a few H atoms and energetic impact of such hydrocarbon ions as well as H^+ ions of a hydrocarbon plasma on a ZnO film may deposit H atoms by forming ZnOH (or hydroxyl groups) and also damage ZnO crystalline structures near its top surface. During ZnO etching by a hydrocarbon plasma, the modification of ZnO by incident H ions/atoms simultaneously occurs with physical impact by C or hydrocarbon ions on the ZnO surface. Since the hydrogen modified layer of ZnO has a higher physical sputtering yield, the sputtering yield of ZnO by a hydrocarbon plasma is typically higher than that by an inert-gas plasmas such as a Ne or Ar plasmas generated under similar conditions.

In this study, we have focused on the effects of hydrogen deposition in ZnO on its sputtering yield. The energetic impact of H^+ ions on ZnO is likely to damage its microcrystalline structures and affect its sputtering yield. How it affects the ZnO sputtering yield is a subject of future study.

ACKNOWLEDGMENTS

[1]J. M. Lee, K. M. Chang, K. K. Kim, W. K. Choi, and S. J. Park, J. Electrochem. Soc. **148**, G1 (2001).

[2]K. Ip, K. H. Baik, M. E. Overberg, E. S. Lambers, Y. W. Heo, D. P. Norton, F. Ren, and J. M. Zavada, Appl. Phys. Lett. **81**, 3546 (2002).

[3]J. S. Park, H. J. Park, Y. B. Hahn, G. C. Yi, and A. Yoshikawa, J. Vac. Sci. Technol., B **21**, 800 (2003).

[4]S. W. Na, M. H. Shin, Y. M. Chung, J. G. Han, and N. E. Lee, J. Vac. Sci. Technol., A **23**, 898 (2005).

[5]Q. Guo, N. Uesugi, T. Tanaka, M. Nishio, and H. Ogawa, Jpn. J. Appl. Phys. **45**, 8597 (2006).

[6]K. Ip *et al.*, Solid State Electron. **47**, 2289 (2003).

[7]H. K. Kim, J. W. Bae, T. K. Kim, K. K. Kim, T. Y. Seong, and I. Adesida, J. Vac. Sci. Technol., B **21**, 1273 (2003).

[8]J. W. Bae, C. H. Jeong, H. K. Kim, K. K. Kim, N. G. Cho, T. Y. Seong, S. J. Park, I. Adesida, and G. Y. Yeom, Jpn. J. Appl. Phys., Part 2 **42**, L535 (2003).

[9]S. J. Pearton, D. P. Norton, K. Ip, Y. W. Heo, and T. Steiner, J. Vac. Sci. Technol., B **22**, 932 (2004).

[10]S. W. Na, M. H. Shin, Y. M. Chung, J. G. Han, S. H. Jeung, J. H. Boo, and N. E. Lee, Microelectron. Eng. **83**, 328 (2006).

[11]W. Lim, L. Voss, R. Khanna, B. P. Gila, D. P. Norton, S. J. Pearton, and F. Ren, Appl. Surf. Sci. **253**, 1269 (2006).

[12]M. H. Shin, M. S. Park, S. H. Jung, J. H. Boo, and N. E. Lee, Thin Solid Films **515**, 4950 (2007).

[13]H. J. Lee, B. S. Kwon, H. W. Kim, S. I. Kim, D. G. Yoo., J. H. Boo, and N. E. Lee, Jpn. J. Appl. Phys., Part 1 **47**, 6960 (2008).

[14]J. C. Woo, G. H. Kim, J. G. Kim, and C. I. Kim, Surf. Coat. Technol. **202**, 5705 (2008).

[15]M. Mehta, M. Ruth, K. A. Piegdon, D. Krix, H. Nienhaus, and C. Meier, J. Vac. Sci. Technol., B **27**, 2097 (2009).

[16]D. Y. Kim, I. C. Hwang, J. Y. Son, and H. J. Kim, J. Korean Phys. Soc. **58**, 1536 (2011).

[17]N. H. Nickel, J. Vac. Sci. Technol., B **18**, 1770 (2000).

[18]S. Veprek, C. Wang, and M. G. J. Veprek-Heijman, J. Vac. Sci. Technol., A **26**, 313 (2008).

[19]Y. Nakakubo, A. Matsuda, M. Fukasawa, Y. Takao, T. Tatsumi, K. Eriguchi, and K. Ono, Jpn. J. Appl. Phys. **49**, 08JD02 (2010).

[20]A. Matsuda, Y. Nakakubo, Y. Takao, K. Eriguchi, and K. Ono, Jpn. J. Appl. Phys., Part 1 **50**, 08KD03 (2011).

[21]G. S. Oehrlein, R. M. Tromp, Y. H. Lee, and E. J. Petrillo, Appl. Phys. Lett. **45**, 420 (1984).

[22]S. A. Vitale and B. A. Smith, J. Vac. Sci. Technol., B **21**, 2205 (2003).

[23]T. Ohchi, S. Kobayashi, M. Fukasawa, T. Kugimiya, T. Kinoshita, T. Takizawa, S. Hamaguchi, Y. Kamide, and T. Tatsumi, Jpn. J. Appl. Phys., Part 2 **47**, 5324 (2008).

[24]T. Ito, K. Karahashi, M. Fukasawa, T. Tatsumi, and S. Hamaguchi, Jpn. J. Appl. Phys., Part 1 **50**, 08KD02 (2011).

[25]S. J. Baik, J. H. Jang, C. H. Lee, W. Y. Cho, and K. S. Lim, Appl. Phys. Lett. **70**, 3516 (1997).

[26]S. Kohiki, M. Nishitani, T. Wada, and T. Hirao, Appl. Phys. Lett. **64**, 2876 (1994).

[27]W. F. Liu, G. T. Du, Y. F. Sun, J. M. Bian, Y. Chen, T. P. Yan, Y. C. Chang, and Y. B. Xu, Appl. Surf. Sci. **253**, 2999 (2007).

[28]B. L. Zhu, J. Wang, S. J. Zhu, J. Wu, R. Wu, D. W. Zeng, and C. S. Xie, Thin Solid Films **519**, 3809 (2011).

[29]P. W. Wang, Y. Y. Chen, J. C. Hsu, and C. Y. Wang, J. Non-Cryst. Solids **383**, 131 (2014).

[30]M. D. McCluskey, S. J. Jokela, K. K. Zhuravlev, P. J. Simpson, and K. G. Lynn, Appl. Phys. Lett. **81**, 3807 (2002).

[31]E. V. Lavrov, J. Weber, F. Börrnert, C. G. Van de Walle, and R. Helbig, Phys. Rev. B **66**, 1 (2002).

[32]S. J. Jokela and M. D. McCluskey, Phys. Rev. B **72**, 113201 (2005).

[33]A. Janotti and C. G. Van de Walle, Nat. Mater. **6**, 44 (2007).

[34]K. Ip *et al.*, Appl. Phys. Lett. **82**, 385 (2003).

[35]H. Li, K. Karahashi, M. Fukasawa, K. Nagahata, T. Tatsumi, and S. Hamaguchi, Jpn. J. Appl. Phys., Part 1 **55**, 021202 (2016).

[36]K. Karahashi and S. Hamaguchi, J. Phys. D: Appl. Phys. **47**, 224008 (2014).

[37]K. Ishikawa, K. Karahashi, H. Tsuboi, K. Yanai, and M. Nakamura, J. Vac. Sci. Technol., A **21**, L1 (2003).

[38]K. Karahashi, K. Yanai, K. Ishikawa, H. Tsuboi, K. Kurihara, and M. Nakamura, J. Vac. Sci. Technol., A **22**, 1166 (2004).

[39]K. Yanai, K. Karahashi, K. Ishikawa, and M. Nakamura, J. Appl. Phys. **97**, 053302 (2005).

[40]T. Ito, K. Karahashi, M. Fukasawa, T. Tatsumi, and S. Hamaguchi, J. Vac. Sci. Technol., A **29** 050601 (2011).

[41]T. Ito, K. Karahashi, K. Mizotani, M. Isobe, S.-Y. Kang, M. Honda, and S. Hamaguchi, Jpn. J. Appl. Phys., Part 1 **51** 08HB01 (2012).

[42]T. Ito, K. Karahashi, S. Y. Kang, and S. Hamaguchi, J. Vac. Sci. Technol., A **31**, 031301 (2013).

[43]H. Li, Y. Muraki, K. Karahashi, and S. Hamaguchi, J. Vac. Sci. Technol., A **33**, 040602 (2015).

[44]H. Li, K. Karahashi, M. Fukasawa, K. Nagahata, T. Tatsumi, and S. Hamaguchi, J. Vac. Sci. Technol., A **33**, 060606 (2015).

[45]K. S. Kim, W. E. Baitinger, J. W. Amy, and N. Winograd, J. Electron Spectrosc. **5**, 351 (1974).

[46]R. Kelly, Nucl. Instrum. Methods **149**, 553 (1978).

[47]K. Fink, Phys. Chem. Chem. Phys. **7**, 2999 (2005).

[48]O. Treutler and R. Ahlrichs, J. Chem. Phys. **102**, 346 (1995).

[49]M. V. Arnim and R. Ahlrichs, J. Comput. Chem. **19**, 1746 (1998).

[50]M. Sierka, A. Hogekamp, and R. Ahlrichs, J. Chem. Phys. **118**, 9136 (2003).

[51]A. Schäfer, H. Horn, and R. Ahlrichs, J. Chem. Phys. **97**, 2571 (1992).

[52]A. Schäfer, C. Huber, and R. Ahlrichs, J. Chem. Phys. **100**, 5829 (1994).

[53]H. Evjen, Phys. Rev. **39**, 675 (1932).

[54]L. Z. Stolarczyk and L. Piela, Int. J. Quantum Chem. **22**, 911 (1982).

[55]L. Piela, J. L. Brédas, and J. M. André, J. Chem. Phys. **78**, 295 (1983).

[56]S. Grimme, J. Antony, S. Ehrlich, and H. Krieg, J. Chem. Phys. **132**, 154104 (2010).

[57]P. A. M. Dirac, Proc. R. Soc., A **123**, 714 (1929).

[58]J. C. Slater, Phys. Rev. **81**, 385 (1951).

[59]J. P. Perdew and Y. Wang, Phys. Rev. B **45**, 13244 (1992).

[60]J. Tao, J. P. Perdew, V. N. Staroverov, and G. E. Scuseria, Phys. Rev. Lett. **91**, 146401 (2003).

[61]R. Ahlrichs, M. Bär, M. Häser, H. Horn, and C. Kölmel, Chem. Phys. Lett. **162**, 165 (1989).

[62]*CRC Handbook of Chemistry and Physics*, 91st ed., edited by W. M. Haynes (Taylor and Francis Group, Boca Raton, FL, 2010–2011).

[63]S. Limpijumnong and S. B. Zhang, Appl. Phys. Lett. **86**, 151910 (2005).